Int j simul model 18 (2019) 3, 543-554
ISSN 1726-4529 Original scientific paper

OPTIMIZATION OF MICRO-TEXTURE DISTRIBUTION THROUGH FINITE-ELEMENT SIMULATION

Wan, Q.[#]; Zheng, M. L.; Yang, S. C. & Sun, J. K.
Harbin University of Science and Technology, Harbin 150080, China
E-Mail: wq@hrbust.edu.cn ([#] Corresponding author)

Abstract
The existing studies on micro-texturing of cutting tools only tackle the micro-textures of uniform distribution. The theoretical and experimental bases are severely lacking for the effects of different micro-texture distributions on the anti-wear and anti-friction properties in titanium alloy cutting. To solve the problem, this paper attempts to explore the wear resistance and friction performance of micro-round-pit (MRP) textures in different distributions. Specifically, the DEFORM-3D finite-element method (FEM) software was adopted to simulate and analyse the effects of these distributions on the ball-end milling of titanium alloy. The simulation shows that the milling force was minimized by the distribution ABC (150-175-200). This result was then confirmed by a milling experiment. In conclusion, the tool wear and cutting friction can be effectively reduced by the optimal micro-texture distribution.
(Received, processed and accepted by the Chinese Representative Office.)

Key Words: Micro-Texture, Finite-Element Method (FEM), Micro-Round-Pit (MRP), Wear Resistance, Friction Performance

1. INTRODUCTION

The wear resistance and friction performance of tools can be improved by machining micro-textures onto the tool surface, thus extending the service life of the tools. The micro-textured tools can work excellently in the cutting of titanium alloy [1, 2]. Out of the various types of micro-textures, the micro-round-pit (MRP) texture boasts the best anti-wear and anti-friction properties, and thus the best cutting quality. To widen the application of titanium alloy, it is necessary to explore the MRP texture and its effects on the cutting of titanium alloy. The finite-element method (FEM), a time- and cost-efficient strategy of numerical simulation, offers a good way for such an exploration. This strategy has been widely adopted for studies on machined geometry [3], tool wear [4], tool surface roughness, and model parameter optimization [5]. Micro-textured tools have been a research hotspot in recent years. For example, Koshy and Tovey [6] designed and fabricated micro-textures on the surface of high-speed steel turning tool, and applied the textured tool to cut aluminium alloy by two different processing methods under lubrication conditions. Zhang et al. [7] examined the cutting performance of a tool coated with TiAlN micro-textures on AISI1045 hardened steel under total and micro-lubrication, revealing that the tool performed better under total lubrication. Kawasegi et al. [8] cut aluminium alloy with a tool textured with micro-grooves under minimum quantity lubrication (MQL), and found that the tool can effectively control the tool-chip friction coefficient, thereby reducing the cutting force and extending the tool life. Enomoto and Sugihara [9] probed into the cutting effects of micro-textured coated tools, and noted that the adhesive wear and surface friction can be reduced by minimizing the contact length of the chip through proper tool positioning. With the aid of DEFORM-3D, Dong et al. [10] simulated the effects of micro-textures on the effective friction coefficient, cutting force and chip flow direction during hard turning, and compared the turning effects between textured and non-textured tools. Ma et al. [11] investigated the depth, edge distance and spacing of micro-textures, and contrasted textured and non-textured tools.

Different numerical simulation methods have been adopted to model the cutting process. For instance, Huang and Liang [12] defined the material properties of workpiece using Oxley's modified Johnson-Cook (J-C) model, and then studied the force and heat of the tool. Moriwaki et al. [13] established a FEM with rigid-plastic features, and used it to simulate the chip formation and the temperature field when the cutting depth falls between millimetres and nanometres. Guo and Liu [14] created FEM-based 2D and 3D models for the cutting process, and simulated the stress and temperature fields of the tool and the chip by the adaptive mesh reconstruction algorithm.

To sum up, the previous studies have detailed how various micro-texture parameters, including shape and size, affect machinability, wear resistance and friction performance. However, the micro-textures are generally distributed uniformly in these studies. The theoretical and experimental bases are severely lacking for the effects of different micro-texture distributions on the anti-wear and anti-friction properties in titanium alloy cutting. Considering the benefits of micro-textures on friction-and-wear resistance, tool life and cutting efficiency, this paper examines the different distributions of the MRP textures, and then simulated the impacts of these distributions on the ball-end milling of titanium alloy. The optimal MRP texture distribution was identified, and verified through milling experiments. Finally, the cutting effects of the optimal distribution were subjected to fuzzy evaluation, yielding the optimal micro-texture design for tool rake face for the milling of titanium alloy.

To date, the FEM has been widely adopted for mechanical research [15-17]. Under different influencing factors, many FEM-based theoretical models have been established for micro-textures, and employed to analyse the stress and heat in the cutting process. Nevertheless, there is no report that verifies the accuracy of such FEM models, which determines the simulation effectiveness. To make up for this gap, this paper sets up a theoretical model of the cutting force and heat in the milling process through repeated experiments, aiming to ensure the authenticity and reliability of the research results.

2. MRP TEXTURE DISTRIBUTIONS

2.1 Distribution area

During the cutting of titanium alloy, the friction between the tools on the tool rake face directly bears on the chip formation, the thermal properties of the cutting force, the tool wear and the quality of the machined surface. Therefore, micro-textures need to be added to the tool-chip contact area, such as to reduce friction, enhance wear resistance and improve cutting performance. As shown in Fig. 1, the tool-chip contact area has two kinds of contacts along the tool-chip contact direction, namely, peak point contact and close contact, both of which affect the friction state of the rake face.

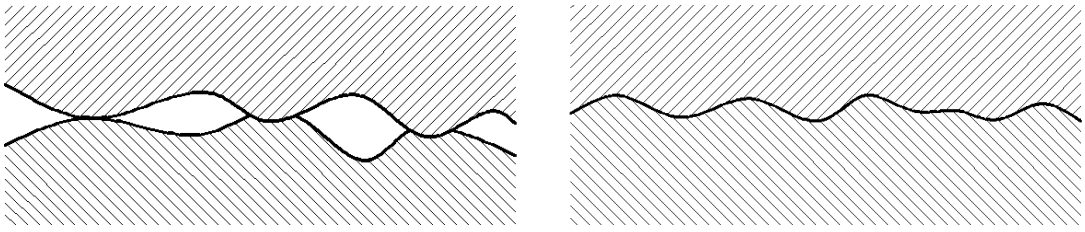

a) Peak point contact b) Close contact

Figure 1: The two types of contact.

The two types of contacts come into being owing to the nonuniform stress distribution. On the tool-chip contact area near the cutting edge, the contact belongs to the close contact under the relatively high stress, and the friction coefficient μ varies from point to point because the

friction does not obey the classical law; on the rake face far away from the cutting edge, the contact belongs to the peak point contact under the relatively small stress, and the friction coefficient is equal at each contact point as the friction follows the classical law. Since close contact contributes most of friction force (85 %) in normal cutting conditions [18], the friction at the rake face mainly comes from the close contact area, which should be highlighted in the research of cutting friction.

To identify the close contact area involved in ball-end milling, a simplified cutting model was established when the machined surface is cylindrical and the trajectory of any point on the cutting edge is approximately circular [19]. The tool-chip contact area is a partial sphere when the feed per tooth f_z is much smaller than the cutting radius R_o of the tool. The tool-chip contact area is illustrated in Fig. 2.

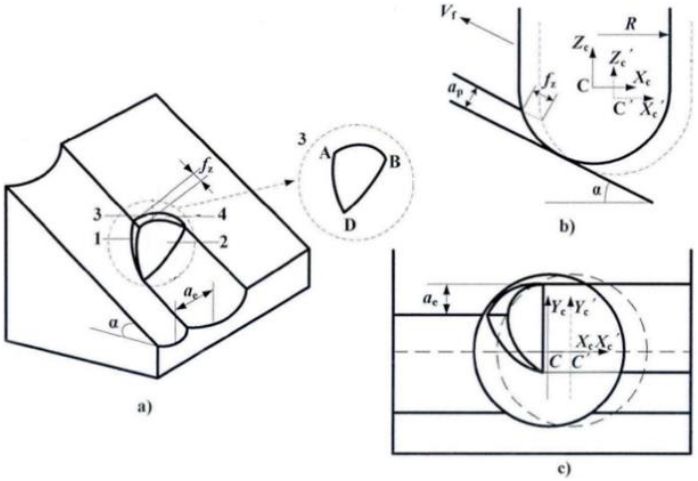

Figure 2: The tool-chip contact area.

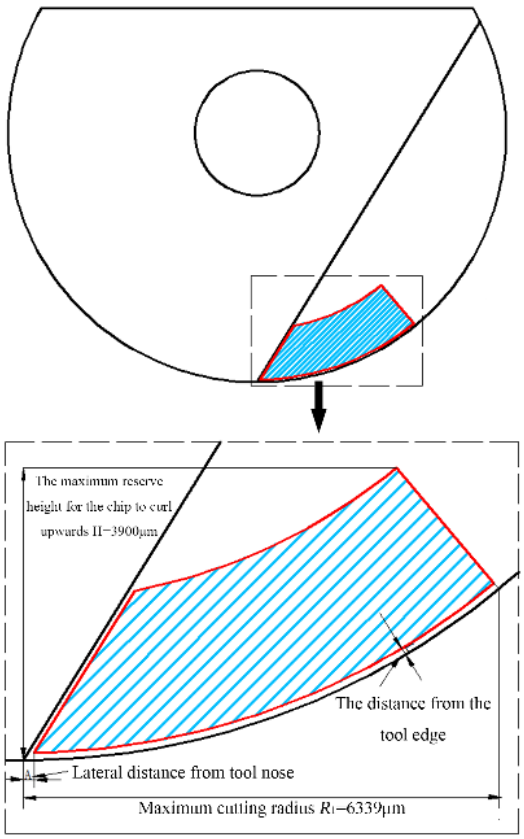

Figure 3: The close contact area.

As shown in Fig. 2 a, the tool-chip contact area is surrounded by the arcs AD, DB and BA, which are formed by intersecting every two lines of the tool surface. The three arcs can be expressed as:

(1) Arc AD:

$$x^2 + 2ya_\varepsilon - a_\varepsilon^2 + z^2 - 2xz\tan\alpha + x^2\tan^2\alpha = 0 \tag{1}$$

(2) Arc DB:

$$-2xf_z\cos\alpha + f_z^2\cos^2\alpha + z^2 - 2zf_z\sin\alpha + f_z^2\sin^2\alpha = 0 \tag{2}$$

(3) Arc BA:

$$x^2 + y^2 + x^2\tan^2\alpha + \frac{2x\tan\alpha\left(R_0 - a_p\right)}{\cos\alpha} + \frac{\left(R_0 - a_p\right)^2}{\cos^2\alpha} - R_0^2 = 0 \tag{3}$$

Fig. 2 b shows the tool-chip contact area on the Xc-Zc plane. The coordinate systems of a tooth and any other tooth are respectively denoted as C'X_c'Y_c'Z_c' and C$X_c$$Y_c$$Z_c$. Fig. 2 c presents the projection for any two adjacent trajectories in the Xc-Yc plane. Then, the close contact area (Fig. 3) can be derived from Eqs. (1) and (3).

2.2 Distribution design of the MRP textures

Fig. 4 shows the cutting effects of the MRP textured tool. The tool-chip contact area can be divided into three areas depending on the distribution of micro-textures. Obviously, Area 1 was more worn than Areas 2 and 3. When the centre-to-centre spacing between the MRP textures remained constant in the tool-chip contact area, only the micro-textures near the cutting edge can resist the wear and friction. The wear- and friction-resistances of the textures weakened as the distribution of the textures moved away from the cutting edge. When in contact with the outflow chip, the textures were distributed in a large area, but the outflow chip was even larger, creating an obvious double cutting phenomenon on the edge of MRP textures. This calls for additional milling force of the tool. Therefore, the uniform micro-texture distribution is not conducive to the anti-friction and anti-wear performance of micro-textures, and may weaken the tool strength. For the purpose of milling, the micro-textures on the tool rake face should be placed at different positions to fulfil different roles.

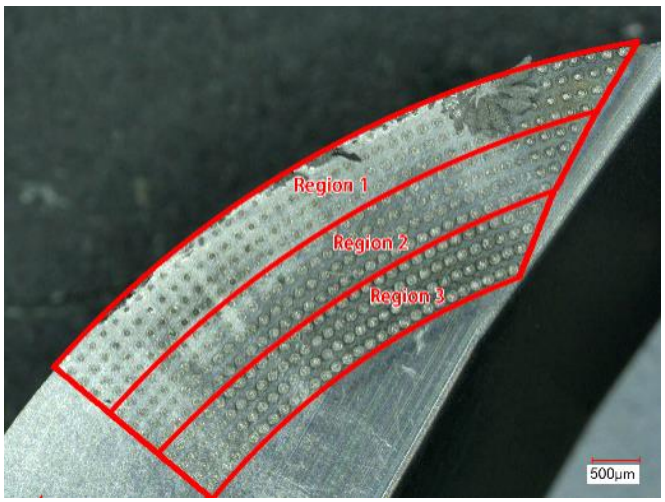

Figure 4: The cutting effects of the MRP textured tool.

In this paper, an MRP texture distribution model is constructed to disclose the wear resistance and friction performance of ball-end millers under nonuniform distribution of micro-textures. First, three micro-texture distribution was defined for each area in Fig. 4,

forming a total of six different micro-texture distributions in the tool-chip contact area. On this basis, the cutting effects of the ball-end miller were experimentally contrasted under three uniform distributions of micro-textures and six nonuniform distributions of micro-textures, with the aim to disclose the effects of different distributions on the friction- and wear-resistances of the ball-end millers. The micro-texture distribution for each area in the tool-chip contact area can be determined accurately according to the above formulas, making it possible to determine the distribution parameters (Fig. 5).

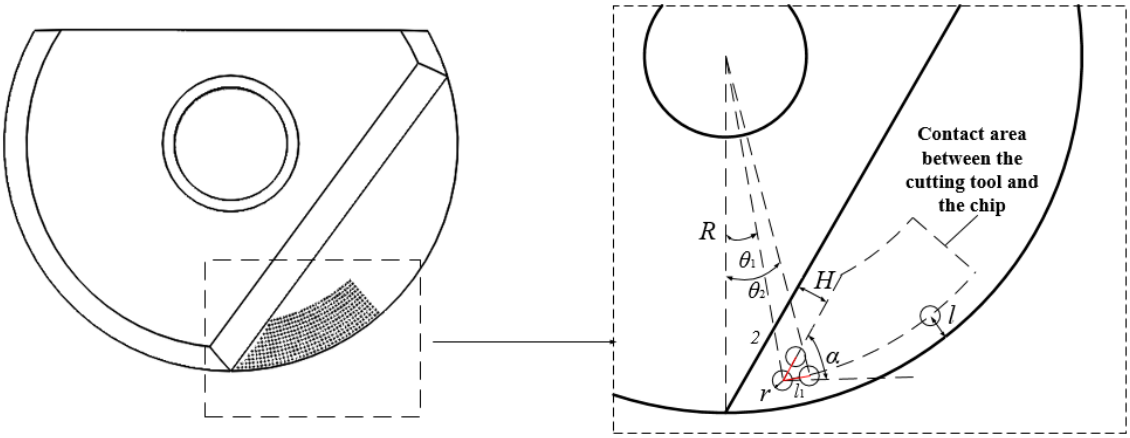

Figure 5: Distribution parameters of the MRP textures.

3. SIMULATION AND RESULTS ANALYSIS

3.1 Construction of geometrical entity model

This subsection attempts to establish a model for milling titanium alloy with a micro-textured ball-end miller. To begin with, a 3D geometrical entity model of the tool and other artefacts were created, and simplified to reduce the simulation complexity without affecting the simulation results.

Fig. 6 describes the initial assembly relationship between the miller and the workpiece. It can be seen that the miller is 10 mm in diameter, 0° in front angle, 11° in rear angle, and 15° in dip angle. The 10 mm × 10 mm × 2 mm workpiece was fed upward along the slope.

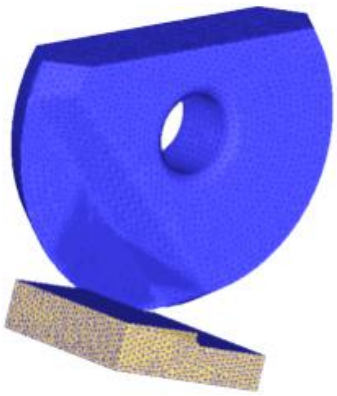

Figure 6: The initial assembly relationship for the miller and the workpiece.

3.2 Construction of the material constitutive model

During the cutting process, the workpiece material suffers from both elastic deformation and plastic deformation, and undergoes property changes like process hardening and thermal softening. The boundary state of the material is highly nonlinear under the joint effect of

plastic yield, flow, hardening, extrusion and friction. Hence, the simulation accuracy relies heavily on the selection of the material constitutive model. Here, the J-C model, an ideal improved model for rigid-plastic materials, is adopted to simulate the exact cutting behaviours:

$$\bar{\sigma} = [A + B\bar{\varepsilon}^{n}]\left[1 + C\ln\left(\frac{\dot{\bar{\varepsilon}}}{\dot{\bar{\varepsilon}}_0}\right)\right]\left[1 - \left(\frac{T - T_0}{T_m - T_0}\right)^{m}\right] \tag{4}$$

where, $\overline{\sigma}$ is the equivalent plastic stress; $\dot{\bar{\varepsilon}}$ is the equivalent plastic strain; $\dot{\bar{\varepsilon}}_0$ is the reference plastic strain; T_0 is the transition temperature; T_m is the melting temperature of the material; *A*, *B*, *C*, *m*, and *n* are the property coefficients of the material. Eq. (4) takes account of the effects of temperature, stress and strain on yield stress.

Here, the tool material is cemented carbide, and the workpiece material is Ti6Al4V titanium alloy. This alloy is sensitive to temperature and strain. Its melting temperature and density are respectively 1,650 °C and 4,440 kg/m^3. The constitutive parameters of the material are listed in Table I below.

Table I: J-C model parameters of Ti6Al4V titanium alloy.

A (MPa)	***B*** (MPa)	***n***	***C***	***m***	T_m (°C)	T_0 (°C)
900.8	890	0.22	0.014	1.1	1650	25

3.3 Construction of the tool-chip contact friction model

The chip-producing friction state in metal cutting is very complicated.

In the process of metal cutting, the friction state regarding the production of chips is very complicated. There are two types of friction forces, namely, the bonding force and the sliding force. The bonding force occurs close to the cutting edge, and relates to the critical shear stress of the material. The sliding force occurs away from the cutting edge, and always remains constant. The two friction forces can be expressed as:

$$\begin{cases} \mu\sigma_{\mathrm{n}} \geq \sigma_{\mathrm{s}} & \tau_{\mathrm{f}} = \sigma_n \\ \mu\sigma_{\mathrm{n}} < \sigma_{\mathrm{s}} & \tau_{\mathrm{f}} = \mu\sigma_n \end{cases} \tag{5}$$

where, τ_f is the frictional shear stress on the tool rake face; σ_s is the maximum shear stress on the workpiece material; σ_n is the normal stress on the tool rake face; μ is the friction coefficient on the tool rake face. If $\mu\sigma_n \geq \sigma_s$, the friction force belongs to the bonding force; if $\mu\sigma_n < \sigma_s$, the friction force belongs to the sliding force. The above model is a modified Coulomb friction model, which has been widely used in the FEM simulation of the milling process.

3.4 Chip separation criteria and mesh generation

Under the action of the tool, chips are separated from the workpiece. Here, a physical criterion and a geometric criterion are created to describe the chip separation from the workpiece [20]. To satisfy the physical criterion, the "contact-penetrating" adaptive mesh generation method of DEFORM-3D was selected to partition the cases that the tool is embedded deep into the workpiece. By this method, it is possible to even out otherwise seriously distorted grids, ensuring the simulation accuracy and convergence. The pre- and post-meshing grids are shown in Fig. 7 below.

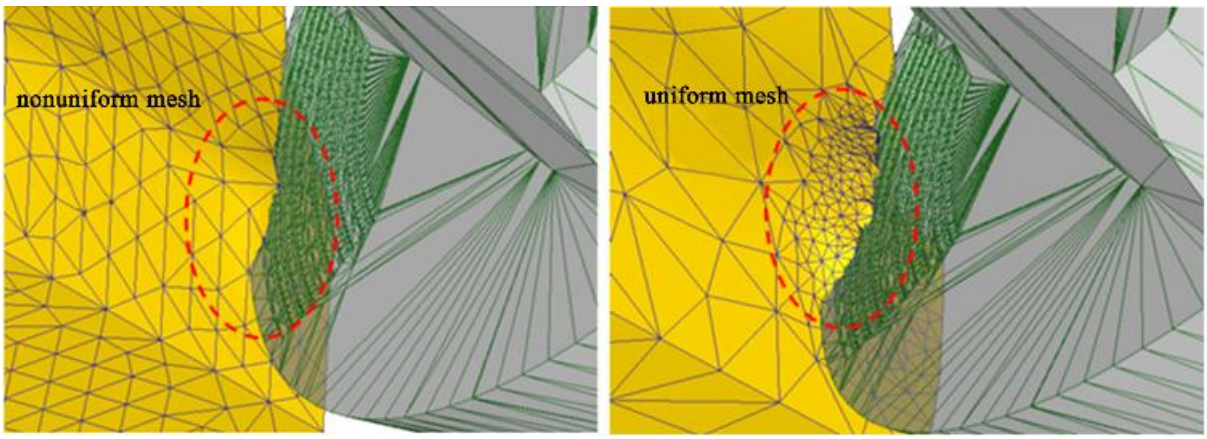

a) Pre-meshing b) Post-meshing

Figure 7: The mesh generation process.

3.5 Generation of cutting heat

The heat release of metal cutting can be described as [21]:

$$k\left[\frac{\partial^2 T}{\partial X^2}+\frac{\partial^2 T}{\partial Y^2}+\frac{\partial^2 T}{\partial Z^2}\right]-\rho c_p\left[\mu\frac{\partial T}{\partial X}+v\frac{\partial T}{\partial Y}+w\frac{\partial T}{\partial Z}\right]+q=0 \tag{6}$$

where, $\dot{q}=\dot{q_p}+\dot{q_f}$ is heat production rate per unit volume; ρ is the material density; k is the heat conduction coefficient; c_p is the specific heat capacity; X, Y, and Z are the coordinates in the Cartesian coordinate system; u, v, and w are the heat source motion components in X, Y and Z directions, respectively.

3.6 Heat transfer and tool wear

The heat transfer between the tool and the workpiece can be described by Cooper's contact heat transfer coefficient formula [22]:

$$h_c=\frac{A\exp\left(-\left[erfc^{-1}1\left(2A_r/A_a\right)\right]^2\right)}{\left(1-\sqrt{A_r/A_a}\right)^{1.5}} \tag{7}$$

where, A_r and A_a are the actual and nominal tool-workpiece contact areas. The heat transfer coefficient was determined as 45 W/m^{2}K according to the actual material conditions. Under the simulation requirements, the tool-wear model in DEFORM-3D can be defined as:

$$w=\int Cv_s\sigma_f e^{-\lambda/T}dt \tag{8}$$

where, w is the wear depth (mm); σ_f is the positive pressure (MPa); v_s is the slip rate of the workpiece relative to the tool (m/s); T is the tool surface temperature; dt is the time increment; $C=0.0000001$; $\lambda=855$.

3.7 Results analysis

Table II lists the simulation and test parameters for the titanium alloy milling by a micro-textured tool. The MRPs with spacing of 150 μm,175 μm and 200 μm, denoted as distribution ABC, were taken as an example for results analysis. The milling forces measured in the simulation are presented in Fig. 8 and the simulation data on the milling force and milling temperature are given in Table III.

Table II: Simulation and test parameters.

Cutter diameter (mm)	**Cutting depth** a_p (mm)	**Cutting width** a_e (mm)	**Cutting speed** v_c (m/min)	**Feed per tooth** f_z (mm/z)	**Speed** n (r/min)
20	0.7	0.5	120	0.08	1910.83

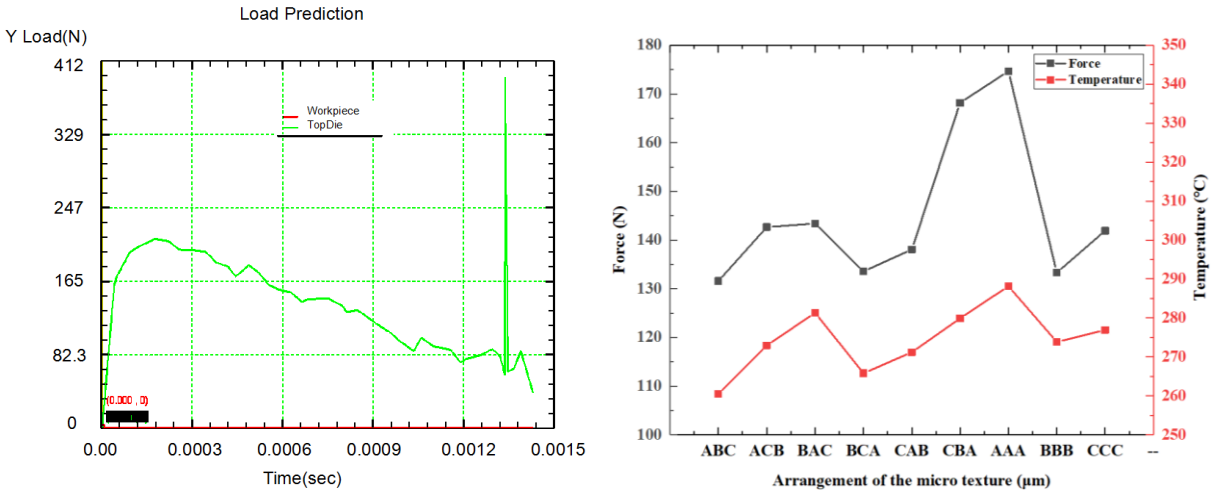

Figure 8: The milling forces measured in the simulation.

It can be seen that the milling force of the tool was minimal when the micro-texture obeyed distribution ABC. This is because the additional micro-textures in Area 1 reduces the contact length and friction between the chip and the cutting face in the close contact area; therefore, the tool-chip contact length decreases in Area 1, where the MRP spacing is minimal and the number of the MRPs is maximal, leading to a decline in the milling force. In Area 2, the micro-textures were deformed, weakening their wear resistance and friction performance. Thus, the secondary cutting of the chip and micro-texture edges can be prevented by increasing the micro-texture spacing, which reduces the number of rows between the textures. In Area 3, the micro-textures had little anti-wear and anti-friction effects. In this case, the distance between adjacent MRPs should be increased to limit the number of micro-textures, such as to reduce the cutting force generated by the chip flow across the edge of each MRP. The distance increase can also enhance the tool strength.

Table III: The simulation data.

Cutting time (s) / **Type of distribution**	3×10^{-4}	6×10^{-4}	9×10^{-4}	12×10^{-4}	**Average cutting force** (N)	**Average temperature** (°C)
ABC	185.50	148.60	111.52	80.75	131.59	260.48
ACB	205.80	166.20	113.60	85.00	142.65	272.96
BAC	194.20	162.00	106.38	111.04	143.41	281.32
BCA	192.50	153.60	121.60	66.56	133.57	265.84
CAB	197.80	156.70	123.65	74.07	138.06	271.20
CBA	234.00	197.60	137.60	103.50	168.18	279.92
AAA	208.00	208.00	163.70	119.06	174.69	288.16
BBB	175.00	157.40	126.63	74.19	133.31	273.84
CCC	192.20	150.20	129.20	96.09	141.92	276.92

Fig. 9 displays the cloud map on the temperature of micro-textured ball-end miller in the cut-in and cut-out processes obtained by SEM simulation, while Fig. 10 shows the cloud map on the cutting temperature of the miller. Obviously, the cutting temperature of the ball-end miller was lower after micro-texturing. The temperature drop is attributable to the growth of heat dissipation area between the tool and chips, thanks to the MRP texturing of the miller rake face. With the increase in pit spacing, the cutting temperature went through three phases: stabilization, decline and increase. As shown in Table III, the cutting temperature reached the minimum when the MRPs obeyed the distribution ABC. The greater the pit spacing, the longer the actual contact of the chip, the more the cutting heat release, and the more severe the friction, and the larger the bonding area.

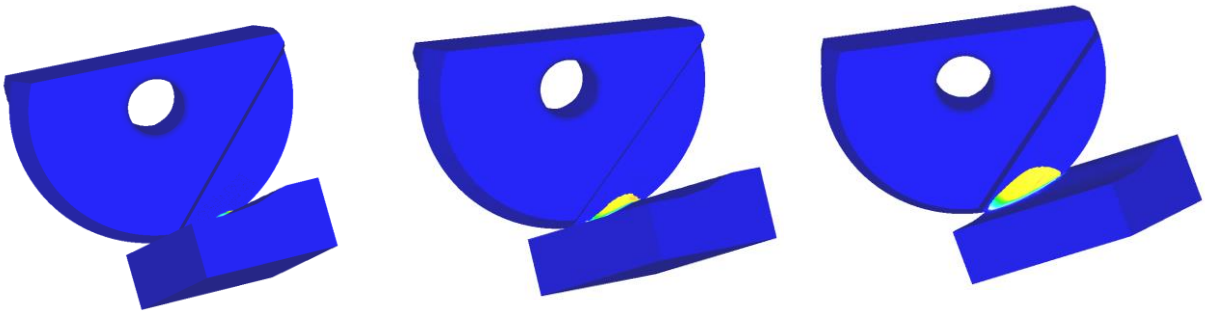

Figure 9: The cloud map on the temperature of micro-textured ball-end miller.

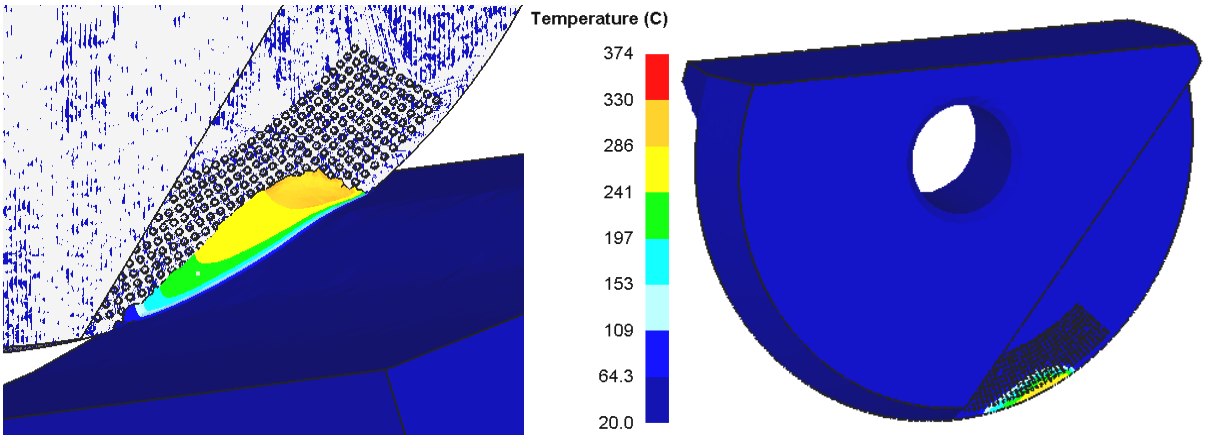

Figure 10: The cloud map on the cutting temperature of micro-textured ball-end miller.

4.EXPERIMENTAL VERIFICATION

The simulation results were verified through an experiment on a YG8 carbide ball-end miller (type: BNM-200; diameter: 20 mm; front angle: 0°; rear angle: 11°). Before the experiment, the miller was micro-textured by fibre laser at the mean laser output power of 50 W, laser processing power of 90 %, scanning speed of 1,000 m/s and scanning frequency of 3 [23]. After laser machining, the miller was cleaned by ultrasonic waves to remove burrs and slags.

A piece of 150 mm × 100 mm × 70 mm titanium alloy TC4 was selected as the workpiece. The milling temperature was collected by an E12-3-K-U thermocouple. Fig. 11 illustrates the experimental environment. To optimize the surface quality of the workpiece, the dip angle of milling was set to 15° [24]. The milling parameters and experimental results are shown in Table II and Table IV, respectively.

Figure 11: The experimental environment.

Table IV: The experimental results.

Number	**Type of micro-texture distribution**	**Cutting force** (N)	**Temperature** (°C)
1	ABC	186.15	142.32
2	ACB	194.53	144.86
3	BAC	198.46	146.30
4	BCA	198.73	152.46
5	CAB	200.79	156.32
6	CBA	203.15	162.76
7	AAA	209.62	164.52
8	BBB	208.99	158.74
9	CCC	204.09	156.53

It can be seen from Table IV that the micro-textures of nonuniform distribution produced better milling force than those of uniform distribution, due to the changes in the distribution density. The secondary cutting at the MRP edges when the chip flows out of the rake face was reduced, thus reducing the milling force. In this case, distribution ABC is the most effective pattern for micro-textures, in that it produced the lowest milling force. This result agrees well with the previous simulation. Comparing the different areas, it is clear that the micro-texturing only enhanced the wear resistance and friction performance in Areas 1 and 2, especially in Area 1. Hence, Area 1 should have the densest distribution of micro-textures, followed by Area 2 and Area 3. This is the best way to optimize the anti-wear and friction effects of micro-textures. The secondary cutting was most serious in Area 3, calling for less dense distribution of micro-textures and fewer MRPs in this area. The sparse distribution could limit the interaction between the edges of the MRPs and the chip, which is the source of secondary cutting, thereby reducing the required milling force.

5. CONCLUSIONS

To determine the micro-texture distribution area, the tool-chip contact area was divided into 3 areas, and a specific micro-texture distribution was defined for each area. Then, the positions and distribution of each type of micro-texture in the tool-chip contact area were identified accurately according to the defining rules of the corresponding distribution. The textures thus fine-tuned lay a basis for quasi-fabrication and exploration of different micro-texture parameters and their impacts on the anti-wear and anti-friction mechanisms.

The distribution ABC (150-175-200) was confirmed as the optimal distribution of the micro-textures on the tool face, which minimizes the milling force, through simulation and experiment. Meanwhile, the author determined the area affected by the anti-wear and anti-friction properties of micro-texturing and that by the secondary cutting. It is learned that micro-texturing only had anti-wear and anti-friction effects in Areas 1 and 2, especially in Area 1. Besides, the severe secondary cutting in Area 3 calls for a different kind of micro-texture distribution.

ACKNOWLEDGEMENTS

This work was financially supported by the National Nature Science Foundation of China (No. 51875144). Thanks especially.

REFERENCES

[1] Cui, X. Y. (2016). *Research on the surface quality of titanium alloy with micro-textured ball-end milling cutter*, Harbin University of Science and Technology, Harbin

[2] Chen, Z. M.; Zhang, J. F.; Feng, P. F.; Wu, Z. J. (2013). A simulation study on the effect of micro-textured tools during orthogonal cutting of titanium alloy Ti-6Al-4V, *Applied Mechanics and Materials*, Vol. 281, 389-394, doi:10.4028/www.scientific.net/AMM.281.389

[3] Deng, W. J.; Li, Q.; Xie, Z. C.; Lin, P. (2013). Numerical analysis of rectangular groove cutting with different RC tools, *International Journal of Simulation Modelling*, Vol. 12, No. 2, 120-131, doi:10.2507/IJSIMM12(2)5.243

[4] Tamizharasan, T.; Senthil Kumar, N. (2012). Optimization of cutting insert geometry using DEFORM-3D: numerical simulation and experimental validation, *International Journal of Simulation Modelling*, Vol. 11, No. 2, 65-76, doi:10.2507/IJSIMM11(2)1.200

[5] Vijay Sekar, K. S.; Pradeep Kumar, M. (2012). Optimising flow stress input for machining simulations using Taguchi methodology, *International Journal of Simulation Modelling*, Vol. 11, No. 1, 17-28, doi:10.2507/IJSIMM11(1)2.195

[6] Koshy, P.; Tovey, J. (2011). Performance of electrical discharge textured cutting tools, *CIRP Annals*, Vol. 60, No. 1, 153-156, doi:10.1016/j.cirp.2011.03.104

[7] Zhang, K.; Deng, J.; Sun, J.; Jiang, C.; Liu, Y.; Chen, S. (2015). Effect of micro/nano-scale textures on anti-adhesive wear properties of WC/Co-based TiAlN coated tools in AISI 316 austenitic stainless steel cutting, *Applied Surface Science*, Vol. 355, 602-614, doi:10.1016/j.apsusc.2015.07.132

[8] Kawasegi, N.; Sugimori, H.; Morimoto, H.; Morita, N.; Hori, I. (2009). Development of cutting tools with microscale and nanoscale textures to improve frictional behaviour, *Precision Engineering*, Vol. 33, No. 3, 248-254, doi:10.1016/j.precisioneng.2008.07.005

[9] Sugihara, T.; Enomoto, T. (2009). Development of a cutting tool with a nano/micro-textured surface-improvement of anti-adhesive effect by considering the texture patterns, *Precision Engineering*, Vol. 33, No. 4, 425-429, doi:10.1016/j.precisioneng.2008.11.004

[10] Dong, M. K.; Bajpai, V.; Bo, H. K.; Hyung, W. P. (2015). Finite element modeling of hard turning process via a micro-textured tool, *The International Journal of Advanced Manufacturing Technology*, Vol. 78, No. 9-12, 1393-1405, doi:10.1007/s00170-014-6747-x

[11] Ma, J.; Hung, D.; Lian, Y.; Lei, S. (2015). Assessment of microgrooved cutting tool in dry machining of AISI 1045 steel, *Journal of Manufacturing Science and Engineering*, Vol. 137, No. 3, Paper 031001, 9 pages, doi:10.1115/1.4029565

[12] Huang, Y.; Liang, S. Y. (2003). Cutting forces modeling considering the effect of tool thermal property-application to CBN hard turning, *International Journal of Machine Tools and Manufacture*, Vol. 43, No. 3, 307-315, doi:10.1016/S0890-6955(02)00185-2

[13] Moriwaki, T.; Sugimura, N.; Luan, S. (1993). Combined stress, material flow and heat analysis of orthogonal micromachining of copper, *CIRP Annals*, Vol. 42, No. 1, 75-84, doi:10.1016/S0007-8506(07)62395-6

[14] Guo, Y. B.; Liu, C. R. (2002). FEM analysis of mechanical state on sequentially machined surfaces, *Machining Science and Technology*, Vol. 6, No. 1, 21-41, doi:10.1081/MST-120003183
[15] Zahan, I.; Alim, M. A. (2018). Effect of conjugate heat transfer on flow of nanofluid in a rectangular enclosure, *International Journal of Heat and Technology*, Vol. 36, No. 2, 397-405, doi:10.18280/ijht.360203
[16] Salloomi, K. N.; Al-Sumaidae, S. (2017). Numerical validation of temperature distribution in friction stir welded aluminum 7075-T651 plates using pseudo heat transfer model, *Annales de Chimie – Science des Matériaux*, Vol. 41, No. 1-2, 29-38, doi:10.3166/ACSM.41.29-38
[17] Amiri, R.; Bouiadjra, B. B.; Amiri, A.; Haref, D. C. (2018). 3D finite element analysis of stem-cement interface under cavity effect, *Revue des Composites et des Matériaux Avancés*, Vol. 28, No. 4, 455-469, doi:10.3166/RCMA.28.455-469
[18] Wu, Z. (2013). *Study on Micro-texture Self-lubricating and Pulsating Heat Pipe Self-cooling Dry Cutting Tools*, Shandong University, Jinan
[19] Yang, S.-C.; Wang, H.-Y.; Zhang Y.-H.; Zhang, L. (2016). Cutting performance evaluation of surface micro-texture ball end milling based on multi-objective decision making, *Journal of Harbin University of Science and Technology*, Vol. 21, No. 6, 1-5
[20] Huang, J. M.; Black, J. T. (1996). An evaluation of chip separation criteria for the FEM simulation of machining, *Journal of Manufacturing Science and Engineering*, Vol. 118, No. 4, 545-554
[21] Moustapha, H. (2018). The relaxation effect on residual stress value in butt-welded X70 steel, *Mathematical Modelling of Engineering Problems*, Vol. 5, No. 3, 232-236, doi:10.18280/mmep.050315
[22] Deng, W.-J.; Xia, W.; Zhou, Z.-Y.; Li, Y.-Y. (2004). Application of finite element method in metal cutting process analysis, *Tool Engineering*, Vol. 16, No. 11, 20-27
[23] Yang, S.-C.; Wang, Z.-W.; Zhang, Y.-H.; Wan, Q.; Cui, X.-Y.; Xie, Y. (2015). Finite element simulation for machining titanium alloy with micro-texture ball-end mill, *Journal of Shenyang University of Technology*, Vol. 37, No. 5, 530-535, doi:10.7688/j.issn.1000-1646.2015.05.10
[24] Zhang, Y. H.; Yang, S. C.; Feng, C. (2016). Research on the tool wear mechanism of cemented carbide ball end mill machining titanium alloy, *Material Science Forum*, Vols. 836-837, 318-325, doi:10.4028/www.scientific.net/MSF.836-837.318